

Bayesian framework for inversion of second-order stress glut moments: application to the 2019 Ridgecrest sequence mainshock

James Atterholt¹ and Zachary E. Ross¹

¹California Institute of Technology

November 22, 2022

Abstract

We present a fully Bayesian inverse scheme to determine second moments of the stress glut using teleseismic earthquake seismograms. The second moments form a low-dimensional, physically-motivated representation of the rupture process that captures its spatial extent, source duration, and directivity effects. We determine an ensemble of second moment solutions by employing Hamiltonian Monte Carlo and automatic differentiation to efficiently approximate the posterior. This method explicitly constrains the parameter space to be symmetric positive definite, ensuring the derived source properties have physically meaningful values. The framework accounts for the autocorrelation structure of the errors and incorporates hyperpriors on the uncertainty. We validate this methodology using a synthetic test and subsequently apply it to the 2019 Mw7.1 Ridgecrest earthquake using teleseismic data. The distributions of second moments determined for this event provide probabilistic descriptions of low-dimensional rupture characteristics that are generally consistent with results from previous studies. The success of this case study suggests that probabilistic and comparable finite source properties may be discerned for large global events regardless of the quality and coverage of local instrumentation.

1 **Bayesian framework for inversion of second-order stress**
2 **glut moments: application to the 2019 Ridgecrest**
3 **sequence mainshock**

4 **James Atterholt¹ and Zachary E. Ross¹**

5 ¹Seismological Laboratory, California Institute of Technology, Pasadena, California, USA 91125

6 **Key Points:**

- 7 • We develop a Bayesian inverse scheme to solve for stress glut second moments of
8 earthquakes using teleseismic data.
9 • We sample the positive-definite constrained posterior distribution using Hamiltonian
10 Monte Carlo sampling and automatic differentiation.
11 • Using the 2019 Ridgecrest sequence mainshock as an example, we demonstrate the
12 efficacy and utility of this inverse framework.

Corresponding author: James Atterholt, atterholt@caltech.edu

Abstract

We present a fully Bayesian inverse scheme to determine second moments of the stress glut using teleseismic earthquake seismograms. The second moments form a low-dimensional, physically-motivated representation of the rupture process that captures its spatial extent, source duration, and directivity effects. We determine an ensemble of second moment solutions by employing Hamiltonian Monte Carlo and automatic differentiation to efficiently approximate the posterior. This method explicitly constrains the parameter space to be symmetric positive definite, ensuring the derived source properties have physically meaningful values. The framework accounts for the autocorrelation structure of the errors and incorporates hyperpriors on the uncertainty. We validate this methodology using a synthetic test and subsequently apply it to the 2019 M_w 7.1 Ridgecrest earthquake using teleseismic data. The distributions of second moments determined for this event provide probabilistic descriptions of low-dimensional rupture characteristics that are generally consistent with results from previous studies. The success of this case study suggests that probabilistic and comparable finite source properties may be discerned for large global events regardless of the quality and coverage of local instrumentation.

Plain Language Summary

Earthquake science is presented with the challenging problem of determining properties of earthquake sources that occur deep within the Earth using observations made at the surface of the Earth. Typically, the process for determining these important quantities involves finding solutions to complicated optimization problems that, given the necessarily poor data coverage, are poorly constrained. With this challenge in mind, we present a framework to solve for some fundamental properties of earthquake sources like spatial extent, rupture propagation direction, and duration. This approach requires few assumptions about the geometry of the fault that ruptured and the dynamics of the rupture process, in contrast to more traditional methods. This procedure also provides a probabilistic description of these earthquake source properties, which is essential, because the uncertainty inherent to this problem dictates that we cannot confidently choose any one particular solution. We demonstrate this method's utility by applying it to the 2019 magnitude 7.1 Ridgecrest earthquake. Through this application, we show that this framework can yield probabilistic and comparable estimations of rupture properties for large global earthquakes using seismic data recorded at great distances.

1 Introduction

Earthquakes are known to exhibit complex rupture processes that vary strongly in space and time. A better understanding of the factors controlling earthquake behavior consequently requires constraining the finite source properties of earthquakes. Today, high dimensional estimates (~ 1000 parameters) of finite source properties are routinely computed for significant earthquakes (e.g. Wald & Heaton, 1992; Ammon, 2005; Moreno et al., 2010; Ide et al., 2011; Ross et al., 2019). These estimates usually involve the inversion for slip on a predefined fault plane using some combination of seismic, geodetic, and tsunami data with kinematic constraints placed on the rupture propagation (Hartzell & Heaton, 1983; Du et al., 1992; Saito et al., 2011). These solutions, termed finite-fault slip distributions, provide a detailed image of time-dependent slip behavior during an earthquake rupture. However, these inversions require often arbitrary parameterization of the source geometry, have a general lack of sensitivity to rupture velocity, and need substantial regularization due to the non-uniqueness of the inverse problem (e.g. Lay, 2018; Wang et al., 2020). This nonuniqueness presents challenges to objectively comparing finite source properties between events, and thus limits our ability to discern patterns in earthquake behavior that could inform a deeper understanding of earthquake phenomenology.

The limitations of routinely computed estimates of finite source properties motivates the development of alternative estimates that overcome these limitations. One potential alternative is the second moment formulation (G. Backus & Mulcahy, 1976a, 1976b), in which higher-order mathematical moments of the stress glut, a source representational quantity, are used to describe basic properties of the rupture process in space and time. Higher-order stress glut moments have been successfully computed in the past (Bukchin, 1995; McGuire et al., 2000, 2001; McGuire, 2002, 2004; Chen, 2005; Meng et al., 2020), but this methodology has received little attention compared to slip inversions. The second-moment formulation yields low-dimensional, physically-motivated estimates of the spatial extent, directivity, and duration of earthquake ruptures. It requires no prior knowledge of the rupture velocity, and makes only mild assumptions about the source geometry. Being free of gridding and associated discretization issues that complicate slip inversions, the second moment formulation can more objectively facilitate comparisons between events, helping to find common patterns. Illuminating these patterns may help address outstanding questions in earthquake science relating to how fault zones may facilitate or impede earthquake ruptures.

In this study, we use the well-studied 2019 M_w 7.1 Ridgecrest earthquake as a vehicle to demonstrate our methodology (e.g. Ross et al., 2019; Barnhart et al., 2019). The wealth of high quality geodetic data and dense seismic instrumentation have been incorporated into numerous finite-fault slip distribution models (Ross et al., 2019; Barnhart et al., 2019; Liu et al., 2019; Xu et al., 2020; Goldberg et al., 2020; Wang et al., 2020; Jin & Fialko, 2020; Yue et al., 2021). Additionally, rapid field response studies have provided high resolution characterizations of the surface fault rupture and displacement (Ponti et al., 2020; DuRoss et al., 2020). Further, other source estimation techniques such as subevent inversion (Jia et al., 2020) and multi-array backprojection (Xie et al., 2021) have yielded additional constraints on the time-dependence of moment release during the mainshock.

Our contributions in this paper are as follows. We develop a Bayesian inverse scheme for second moments using teleseismic data. We employ Hamiltonian Monte Carlo sampling and automatic differentiation to efficiently sample from the posterior distribution. In doing so, we apply a set of transformations that ensure positive definiteness of the second moments. We demonstrate the efficacy of our methodology by applying the inversion scheme to the Ridgecrest mainshock. We show that our methodology is useful for determining probabilistic and comparable descriptions of low-dimensional rupture parameters with few a priori assumptions.

95 **2 Preliminaries**

Because an earthquake is constituted by a localized zone of inelastic deformation, we can represent the source region as a localized departure from elasticity. These departures can be quantified using the so-called stress glut, $\mathbf{\Gamma}$, the tensor field computed by applying an idealized Hooke's law to the inelastic component of strain in a system (G. Backus & Mulcahy, 1976a, 1976b). The stress glut is nonzero only within the source region. The stress glut is a complete representation of a seismic source in space and time that can be used to reproduce displacements everywhere on Earth for an arbitrary source (Dahlen & Tromp, 1998). Given the typically sparse distribution of seismic observations, solving for the full stress glut is an ill-posed problem. We can simplify the stress glut by assuming the source geometry is constant in space and time:

$$\Gamma_{ij}(\boldsymbol{\xi}, \tau) = \hat{M}_{ij} f(\boldsymbol{\xi}, \tau) \tag{1}$$

96 Where is $\hat{\mathbf{M}}$ is the normalized mean seismic moment tensor and f is the scalar function
 97 defined at the position $\boldsymbol{\xi}$ and time τ . This approximation reduces the solution from a tensor
 98 field to a scalar field and is most valid for seismic sources with stable source mechanisms.

99 We can further reduce the dimensionality of the stress glut by first recognizing that
 100 any scalar function in a bounded interval may be uniquely determined by its collection of
 101 polynomial moments. Because f captures a static displacement, f is nonzero for infinite
 102 time and thus occupies an unbounded interval, but \dot{f} vanishes to zero at the cessation of
 103 rupture and is thus captured within a bounded interval. Hence, considering that the stress
 104 glut prescribes displacements due to an arbitrary seismic source, we can represent seismic
 105 displacements as the superposition of the spatiotemporal moments of the rate function \dot{f} .
 106 We represent the spatial and temporal components of these moments separately, with spatial
 107 order m and temporal order n . At low frequencies, we can truncate this infinite series such
 108 that we only include terms with moments of order $m + n \leq 2$. We can then explicitly define
 109 the measured displacements for a station i at low frequencies as:

$$\begin{aligned} u_i(\mathbf{r}, t) = & \dot{f}^{(0,0)}(\boldsymbol{\xi}^c, \tau^c) \hat{M}_{jl} \frac{d}{d\xi_l} \int_{-\infty}^{+\infty} G_{ij}(\boldsymbol{\xi}^c, \tau^c, \mathbf{r}, t) dt \\ & - \dot{f}_x^{(1,1)}(\boldsymbol{\xi}^c, \tau^c) \hat{M}_{jl} \frac{d}{d\xi_x} \frac{d}{d\xi_l} G_{ij}(\boldsymbol{\xi}^c, \tau^c, \mathbf{r}, t) \\ & + \frac{1}{2} \dot{f}_{xy}^{(2,0)}(\boldsymbol{\xi}^c, \tau^c) \hat{M}_{jl} \frac{d}{d\xi_x} \frac{d}{d\xi_y} \frac{d}{d\xi_l} \int_{-\infty}^{+\infty} G_{ij}(\boldsymbol{\xi}^c, \tau^c, \mathbf{r}, t) dt \\ & + \frac{1}{2} \dot{f}^{(0,2)}(\boldsymbol{\xi}^c, \tau^c) \hat{M}_{jl} \frac{d}{d\xi_l} \frac{d}{dt} G_{ij}(\boldsymbol{\xi}^c, \tau^c, \mathbf{r}, t) \end{aligned} \tag{2}$$

110 Where \mathbf{G} is a Green's tensor prescribing the path effects from a source with the centroid
 111 location $\boldsymbol{\xi}^c$ and centroid time τ^c to an arbitrary station with the location \mathbf{r} at time t , and
 112 $\dot{f}^{(m,n)}(\boldsymbol{\xi}^c, \tau^c)$ is the moment of the scalar rate function $\dot{f}(\boldsymbol{\xi}, \tau)$ of spatial order m and tem-
 113 poral order n taken about the source centroid in space and time (Bukchin, 1995). Equation
 114 2 is only valid at low-enough frequencies, and the determination of "low-enough" depends
 115 on the spatiotemporal dimensions of the source.

116 Several of the moments are of routine use in seismology, while the rest are worked with
 117 sparingly. The moment of order $m + n = 0$ is the scalar moment of the source. The moments
 118 of order $m + n = 1$ correspond to the spatial ($m = 1$) and temporal ($n = 1$) centroids of the
 119 source. Perhaps unfamiliar are the moments of order $m + n = 2$; these moments describe
 120 low-dimensional finite properties of earthquake sources. In particular, $\dot{f}^{(2,0)}(\boldsymbol{\xi}^c, \tau^c)$ is the
 121 spatial covariance of the stress glut, $\dot{f}^{(1,1)}(\boldsymbol{\xi}^c, \tau^c)$ is the spatiotemporal covariance of the
 122 stress glut, and $\dot{f}^{(0,2)}(\boldsymbol{\xi}^c, \tau^c)$ is the temporal variance of the stress glut. These so-called
 123 second moments yield low-dimensional, physically-motivated approximations of the source
 124 volume, source directivity, and source duration respectively (G. E. Backus, 1977).

125 To understand the physical significance of these second moments, we emphasize that
 126 the spatial second moments and the temporal second moments are covariances and variances
 127 respectively. From these quantities we can thus obtain the standard deviation of the stress-
 128 glut distribution, and the standard deviation is a measure of the width of the distribution.
 129 We can then define characteristic dimensions of the source using standard deviations of the
 130 stress glut derived from the second moments (G. E. Backus, 1977; Silver & Jordan, 1983).
 131 These characteristic dimensions may be defined using a metric of ± 1 standard deviation
 132 from the centroid:

$$r^c(\hat{\mathbf{n}}) = \sqrt{\hat{\mathbf{n}}^T \cdot [\dot{f}^{(2,0)}(\boldsymbol{\xi}^c, \tau^c) / \dot{f}^{(0,0)}(\boldsymbol{\xi}^c, \tau^c)] \cdot \hat{\mathbf{n}}},$$

$$t^c = 2\sqrt{\dot{f}^{(0,2)}(\boldsymbol{\xi}^c, \tau^c) / \dot{f}^{(0,0)}(\boldsymbol{\xi}^c, \tau^c)}, \quad (3)$$

133 Where $r^c(\hat{\mathbf{n}})$ is the extent of the characteristic volume from the centroid in the direction of
 134 arbitrary unit vector $\hat{\mathbf{n}}$ and t^c is the characteristic duration of the source. We'll also define
 135 a characteristic length of the source, L^c , as $2 \cdot r^c(\boldsymbol{\eta})$, where $\boldsymbol{\eta}$ is the principal eigenvector of
 136 $\dot{f}^{(2,0)}(\boldsymbol{\xi}^c, \tau^c)$. Using the mixed second moments and the characteristic dimensions described
 137 in equation 3, we can get estimates of the velocity of the rupture:

$$\mathbf{v}_0 = \dot{f}^{(1,1)}(\boldsymbol{\xi}^c, \tau^c) / \dot{f}^{(0,2)}(\boldsymbol{\xi}^c, \tau^c),$$

$$v^u = L^c / t^c \quad (4)$$

138 Where \mathbf{v}_0 is the average instantaneous velocity of the centroid of the rupture and v^u is an
 139 upper bound on the average velocity of the rupture. The quantities described in equations
 140 3 and 4 thus yield physically interpretable values with which we can evaluate and compare
 141 stress glut second moment solutions and contextualize these solutions in the broader source
 142 characterization literature.

143 3 Methods

144 3.1 Data and Preprocessing

145 In this study we work with both real and synthetic seismic waveform data. The real
 146 data are vertical component seismic data from 48 Global Seismographic Network (GSN)
 147 stations (Figure 1). We selected these stations both by the source-to-receiver distance
 148 and by evaluating how well the waveforms were approximated by point source synthetics
 149 computed using the gCMT solution. The seismograms used in the inversion are 700 second
 150 windows about the surface wave packet that we manually selected from 7200 second windows
 151 that start at the gCMT centroid time for the Ridgecrest mainshock. In this study, we only
 152 use the vertical component of the seismograms and only include R1 arrivals. The addition of
 153 other phases like G1 arrivals and body waves, as well as R2 and G2 arrivals, would further
 154 constrain the posterior distribution, but we reserve the inclusion of these additional phases
 155 for future studies. We down-sample the waveform data to a 0.05 Hz sampling rate, which
 156 reduces the correlation between samples and minimizes the computational demands of the
 157 inversion. As part of the construction of the forward propagation matrix, we computed the
 158 Green's tensor using the gCMT moment tensor and centroid location, which we perturbed
 159 to compute the requisite spatial derivatives numerically.

160 To compute the Green's tensor, we use the 3D Earth model S362ANI + M (Moulik &
 161 Ekström, 2014) and the full waveform modeling software Salvus (Afanasiev et al., 2019),
 162 which employs the spectral element method to simulate wave propagation. After computing

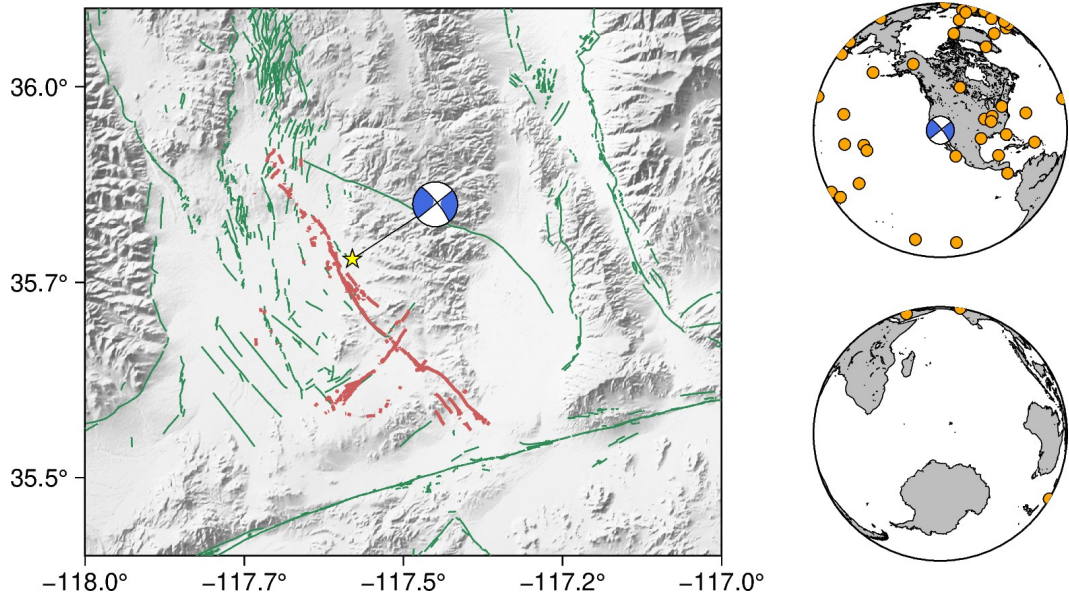


Figure 1. Left: Geographic setting of the 2019 Ridgecrest Sequence. Focal mechanism is the gCMT solution for the sequence mainshock. Yellow star indicates the gCMT solution centroid position. Green and red lines indicate USGS mapped quaternary faults (USGS & CGS, 2021) and faults that were activated during the Ridgecrest Earthquake sequence (Ross et al., 2019). The strike, dip, and rake of the true nodal plane as given by the gCMT solution are 321° , 81° , and 180° respectively. Map coloring is reflective of elevation. Right: Global distribution of stations from which waveforms were used in this study.

163 this Green's tensor, we initially keep these waveforms at a high frequency (4 Hz) to improve
 164 numerical stability when approximating integrals and derivatives. We take the necessary
 165 temporal and spatial derivatives and integrals of this Green's tensor numerically using a
 166 centered finite difference approximation. For the spatial derivatives, we tested numerous
 167 finite difference offsets from the spatial centroid using synthetic tests, which are described
 168 subsequently. Given these tests, we prefer a perturbation distance of 250 m because this
 169 distance is both small enough to yield a reasonable approximation of the spatial derivative
 170 and large enough to be numerically stable. The construction of the forward propagation
 171 matrix, which we describe subsequently, requires both the gCMT moment tensor and the
 172 Green's tensor derivatives and integrals.

173 A particularly important step in the preprocessing of these waveforms is selecting which
 174 frequency band to use in the inversion. There are two key issues that need to be balanced
 175 when making this determination. Firstly, equation 2 is a low frequency approximation; at
 176 higher frequencies, moments of order $m + n > 2$ become more significant. This means that
 177 the frequency band needs to be low enough such that we exclude moments of order $m + n > 2$,
 178 or else the inversion will be biased by these higher-order terms. Secondly, moments of order
 179 $m + n = 0$ and $m + n = 1$ are used. The values used for these lower-order terms are robust,
 180 but are subject to error. Thus, we need to ensure that the contributions from moments of
 181 order $m + n = 2$ are large enough such that they exceed the magnitude of error of the lower
 182 order terms, otherwise the inversion will be dominated by this error. In short, the frequency
 183 band should be high enough such that the contribution of the second moments markedly
 184 exceeds the error on the solutions for the zeroth and first moments, and be low enough such
 185 that the contribution of the third moments is reasonably small. A good metric by which to
 186 make this selection is to use the observation that the contribution of moments of order $m + n$

187 is approximately proportional to $(D/P)^{m+n}$ (assuming $(D/P) < 1$) where D is the source
 188 duration and P is the period (G. E. Backus, 1977). Looking at the distribution of scalar
 189 moment estimations for the Ridgecrest mainshock obtained using teleseismic data (GCMT,
 190 2019; USGS, 2019; Liu et al., 2019), we likely approach the order of the error on the zeroth
 191 moment when the contribution of the second moments exceeds 5% of the zeroth moment.
 192 To obtain a period band where the second moments are significant compared to the error
 193 on the lower-order terms and the contribution of the higher-order terms are always small
 194 compared to the second moments, we select a period band that obeys both $(D/P)^2 > 0.05$
 195 and $(D/P)^3 < 0.05$. Taking 25 s as an approximate source duration for the Ridgecrest
 196 mainshock, this yields a period band of 70-110 s. Since source durations are routinely
 197 estimated for global events (e.g. Vallée & Douet, 2016), this method of frequency-band
 198 selection is applicable to most other global events.

199 We only use stations in the distance range $10 - 90^\circ$, with the exception of a few stations
 200 with exceptional fits at distances just above 90° (see Figure 1), to minimize the bias imposed
 201 by the integrated effect of Earth model error. We then align the Green's tensor and observed
 202 displacements of the remaining stations via cross correlation and select a 700 s window that
 203 encompasses the surface wave packets at each station. The time shifts, which are intended to
 204 correct for time errors due to variable Earth model inaccuracy, are performed at a frequency
 205 band at which the third moments are small. There is thus assumed to be minimal skewness in
 206 the source time function, and we then expect the cross-correlation to account for the Earth-
 207 model effected timing error without misaligning the centroid time. We apply a Hamming
 208 taper to the surface wave packet to minimize the contributions of signal at the start and
 209 end of the time window. These time windows constitute the time-segments of the Green's
 210 tensor and data. Because the contribution of moments of order $m + n = 2$ should still be
 211 relatively small in the selected frequency band, the synthetic waveforms produced using a
 212 point source approximation should be similar to the observed waveforms. We thus perform
 213 an additional manual quality control of the remaining stations, and we remove stations that
 214 show a poor match between the data and the point source waveforms. Both the waveforms
 215 that were kept and the waveforms that were thrown out in the course of this quality control
 216 are shown in Figure S1.

217 Before applying this methodology to real data, we will show a test of the outlined inver-
 218 sion procedure using a synthetic source. For this test, we prescribe a 55×15 km rectangular
 219 fault with a strike and dip corresponding to the nodal plane of the gCMT solution associated
 220 with the true rupture surface. We then define a grid of point sources, each with the gCMT
 221 source mechanism and equal fraction of the gCMT moment, along this prescribed fault such
 222 that the spatial release of moment can be approximated as uniform distributions of moment
 223 release along the strike and dip of the fault. We delay the activation of these point sources
 224 according to a prescribed rupture velocity of 2.5 km/s along strike, resulting in an event
 225 duration of 22 s, such that the moment release with time can also be approximated as a
 226 uniform distribution. Using the fact that the width of a uniform distribution is equal to
 227 $2\sqrt{3}\sigma$, where σ is the standard deviation of the Gaussian approximation of that uniform
 228 distribution, we can determine the true second moment solution for this synthetic source.

229 3.2 Inversion

Equation 2 describes the forward model for a second moment tensor source. While it
 appears unruly, many of the terms that constitute it are easily accessible. For a given source,
 we can observe $u_i(\mathbf{r}, t)$ using seismic instrumentation; we can solve for \mathbf{G} , \mathbf{M} , and $(\boldsymbol{\xi}^c, \tau^c)$
 using routine techniques; and we can compute the necessary derivatives and integrals using
 numerical methods. Thus, in equation 2, only the moments of the scalar function f are
 unknown. We can then pose equation 2 as a linear inverse problem:

$$\mathbf{d} = \mathbf{Fp} \tag{5}$$

230 where \mathbf{d} is a vector of measured displacements, \mathbf{F} is a forward propagation matrix of spatial
 231 and temporal integrals and derivatives of \mathbf{G} , the columns of which are weighted by the
 232 components of \mathbf{M} , and \mathbf{p} is a vector of parameters which constitute the lower-order moments
 233 of the stress glut.

234 Numerous Bayesian methods for source parameter inversion have been proposed for
 235 problems such as focal mechanism estimation (Wéber, 2006; Walsh et al., 2009; Lee et al.,
 236 2011; Duputel et al., 2014) and finite-fault slip distribution estimation (Monelli et al., 2009;
 237 Minson et al., 2013). Bayesian inference has been growing increasingly popular because it
 238 provides an ensemble of solutions that are informed by both data and prior distributions
 239 determined by physical constraints or ground truth. The Bayesian formulation described
 240 here allows for the computation of an ensemble of second moment solutions, with each
 241 providing a low dimensional estimate of the source process.

The posterior distribution for this problem can be written as follows (e.g. Tarantola,
 2005),

$$p(\mathbf{p}, \sigma | \mathbf{d}) \propto p(\mathbf{d} | \sigma, \mathbf{p}) p(\sigma) p(\mathbf{p}), \quad (6)$$

242 where σ is a hyperparameter. For the likelihood term, $p(\mathbf{d} | \sigma, \mathbf{p})$, we use a multivariate
 243 normal distribution,

$$p(\mathbf{d} | \sigma, \mathbf{p}) \propto \frac{1}{\sqrt{|\Sigma|}} \exp\left(-\frac{1}{2}(\mathbf{d} - \mathbf{F}\mathbf{p})^T \Sigma^{-1} (\mathbf{d} - \mathbf{F}\mathbf{p})\right) \quad (7)$$

244 Since the observations are time-series data, errors in the forward model will be subject to
 245 temporal autocorrelation. We can account for this correlation structure through the data
 246 covariance matrix, Σ , as outlined in (Duputel et al., 2014). If d_i and d_j are measured
 247 displacements that are on the same trace and are recorded by the same station:

$$\Sigma_{ij} = \sigma \cdot \exp(-|i - j|\delta t / \Delta t) \quad (8)$$

248 Where σ is the hyperparameter included in equations 6 and 7, δt is the sampling rate, and Δt
 249 is the period of the shortest period information included in the time-series. This prescribes
 250 a block diagonal matrix where the blocks have the same length as the time windows taken
 251 from each station. This correlation structure accounts for temporal correlation in the errors,
 252 but not any spatial correlation. In this paper we assume that the observations are spatially
 253 distributed sparsely enough that spatially-correlated errors are negligible.

254 We use uninformed priors in this case study, but note that informed priors can easily be
 255 incorporated (Gelman et al., 2010). That is, with the physical interpretation of the second
 256 moment properties that we will describe shortly, priors on the spatial extent, directivity,
 257 and duration may be imposed given observational ground truth. For example, if the true
 258 nodal plane of an earthquake is known, Gaussian priors may be placed on the spatial second
 259 moment parameters to restrict the principal eigenvector of the spatial covariance matrix to
 260 abut the true nodal plane.

261 The total number of parameters in this inverse problem is 11, and we approximate
 262 $p(\mathbf{p}, \sigma | \mathbf{d})$ using Markov Chain Monte Carlo (MCMC) sampling to obtain an ensemble of
 263 solutions. We do not solve for the zeroth or first order moments, and instead use the gCMT
 264 solution as our moment tensor and centroid location. Future work will focus on jointly
 265 solving for the lower order moments together with the second moments. As the parameter
 266 space is too large for efficient inference with standard Metropolis-Hastings type samplers,
 267 we instead sample from the posterior distribution using Hamiltonian Monte Carlo (HMC)
 268 sampling (Neal, 2010), which is an instance of the Metropolis-Hastings algorithm that can
 269 efficiently sample large parameter spaces using principles from Hamiltonian dynamics. This
 270 is accomplished in part by incorporating gradient information into the sampling process;

271 however, it requires a means to also compute gradients efficiently. Here, we accomplish this
 272 through the use of reverse-mode automatic differentiation (Innes, 2019).

273 For each Markov chain in the inversion, we draw 5000 samples from the posterior dis-
 274 tributions after drawing 5000 burn-in samples. The momentum distribution has a diagonal
 275 mass matrix and the samples are updated using an ordinary leapfrog integrator (Neal, 2010).
 276 To evaluate convergence, we run at least 3 chains of the inversion and compute the Gelman-
 277 Rubin diagnostic using the computed set of chains (Gelman & Rubin, 1992). That is, we
 278 compare the variability within chains to the variability between chains to determine if the
 279 chains all converge to the same target distributions.

280 Additionally, as described in prior work on this subject (Bukchin, 1995; McGuire et
 281 al., 2001), the second moments of the stress glut are covariances, and therefore only a
 282 subset of the parameter space produces valid solutions. Specifically, the second moments
 283 are symmetric positive definite,

$$\mathbf{X} = \begin{bmatrix} \dot{f}^{(2,0)}(\boldsymbol{\xi}^c, \tau^c) & \dot{f}^{(1,1)}(\boldsymbol{\xi}^c, \tau^c) \\ \dot{f}^{(1,1)}(\boldsymbol{\xi}^c, \tau^c)^T & \dot{f}^{(0,2)}(\boldsymbol{\xi}^c, \tau^c) \end{bmatrix} \succeq 0. \quad (9)$$

284 Physically, this is equivalent to saying that the spatial extent and duration of the source are
 285 both non-negative. Typically, when performing a constrained Bayesian inversion, the easiest
 286 course of action is to sample under an unconstrained parameter space and subsequently
 287 transform those parameters into the necessarily constrained parameter space (Gelman et al.,
 288 2010). To this end, we note that, by the Cholesky Factorization Theorem, every symmetric
 289 positive-definite matrix can be decomposed into the product of some lower triangular matrix
 290 with a positive diagonal and the transpose of that same lower triangular matrix. This means
 291 that given \mathbf{X} , there exists a lower triangular matrix \mathbf{L} with positive diagonal components
 292 such that:

$$\mathbf{X} = \mathbf{L}\mathbf{L}^T \quad (10)$$

293 Thus, we can sample freely from the unconstrained off-diagonal components of \mathbf{L} and from
 294 the natural logarithm of the diagonal components of \mathbf{L} . Then, to evaluate our sample against
 295 our data, we can simply build \mathbf{L} using our sample components and then construct \mathbf{X} us-
 296 ing equation 10. From \mathbf{X} we can extract a valid \mathbf{p} with which we evaluate the likelihood
 297 of our sample. A keen observer may notice that while \mathbf{X} need only be symmetric posi-
 298 tive semi-definite, the Cholesky factorization forces \mathbf{X} to be positive definite. In practice,
 299 this distinction is inconsequential, as a positive semi-definite \mathbf{X} suggests that at least one
 300 dimension of the source is identically zero, which will never be true in reality.

4 Results

We first perform our inversion on the synthetic test described in the Methods section. In the interest of evaluating the resolvability of parameters for the Ridgecrest mainshock, we invert for these second moments using the same distribution of stations and the same windowing procedure that we use for the real event. For this test, we also use the mean σ from the to-be-described inversion of real data so we can test this inversion in the presence of realistic error. The marginal probability distributions for each parameter and the joint probability distributions for each pair of parameters are shown in Figure 4. These plots show that most of the parameters are either uncorrelated or weakly correlated with each other, with the exception of some weak correlation between some closely-related spatial variables and some spatial variables with the temporal variable. These plots also show that almost all the components of the expected second moment covariance matrix fall well within the ensemble of solutions, with the exception of a slight underestimate of the magnitude of the north component of the mixed second moment. This discrepancy may be due to the imperfect assumption of uniform moment release with time for this test due to the discretization of the source.

We can further test the fidelity of our inversion results by computing synthetic waveforms using equation 2 and evaluating the fit to the observed waveforms generated for this synthetic example. The waveforms for an ensemble of second moment solutions from a single chain for the synthetic test are shown for a subset of stations with a large diversity of azimuths and distances in Figure 3. The waveform fits match the synthetic observations very well, particularly when the full ensemble of solutions is considered. As is shown in this figure, the inclusion of the inverted-for second moments of the stress glut perturb the point-source waveforms to fit the synthetic observations, thus successfully accounting for the finiteness of the source.

In order to represent the second moment solutions for the synthetic test in a more physically interpretable way, we convert the ensembles of second moments into ensembles of L^c , t^c , $|\mathbf{v}_0|$, and v^u . Additionally, because the directions associated with L^c and $|\mathbf{v}_0|$ are important, we consider the strike (θ) and plunge (ϕ) associated with these quantities as well. We plot the ensembles of these quantities in Figure 4. We find that the ensembles of these converted parameters are largely normally distributed, and the values associated with the anticipated solution for the synthetic test all fall within these ensembles.

Now, we invert for the second moments of the 2019 Ridgecrest mainshock using the real data. The distributions of the 10 independent parameters of the second moments for a single chain of the inversion using the real data are shown in Figure 5. We run the inversion for a set of chains, shown in Figure S2, and compute the Gelman-Rubin diagnostic (Gelman & Rubin, 1992) using these chains. The Gelman-Rubin values are far less than 1.1, suggesting that the chains have converged to the target posterior distributions for the second moments. The joint probability distributions for each pair of parameters are shown in Figure 5. As with the synthetic test, these joint distributions show that the inverted parameters are mostly uncorrelated with each other. Some of the marginal distributions of the second moments are skewed due to the positive-definite constraint placed on the inversion. The distribution for the hyperparameter σ is shown in Figure S3. We can also evaluate the waveform fits for the inversion using real data. A representative subset of these waveform fits is shown in Figure 6. The computed waveforms for the ensemble of solutions inverted for under this framework fit the observed waveforms reasonably well.

Using these ensembles of second moments, we can summarize the physical parameters of the Ridgecrest mainshock. We show these distributions in Figure 7. As with the synthetic test, most of these ensembles are normally distributed, with the exception of ϕ^{L^c} , which is bimodal, which reflects some nonlinearity in the mapping between the raw second moments and the derived parameters. We find that, within two standard deviations, the characteristic length of the rupture is 47.3 ± 6.0 km with strike and plunge of $327.7 \pm 7.5^\circ$ and $-0.2 \pm 9.1^\circ$

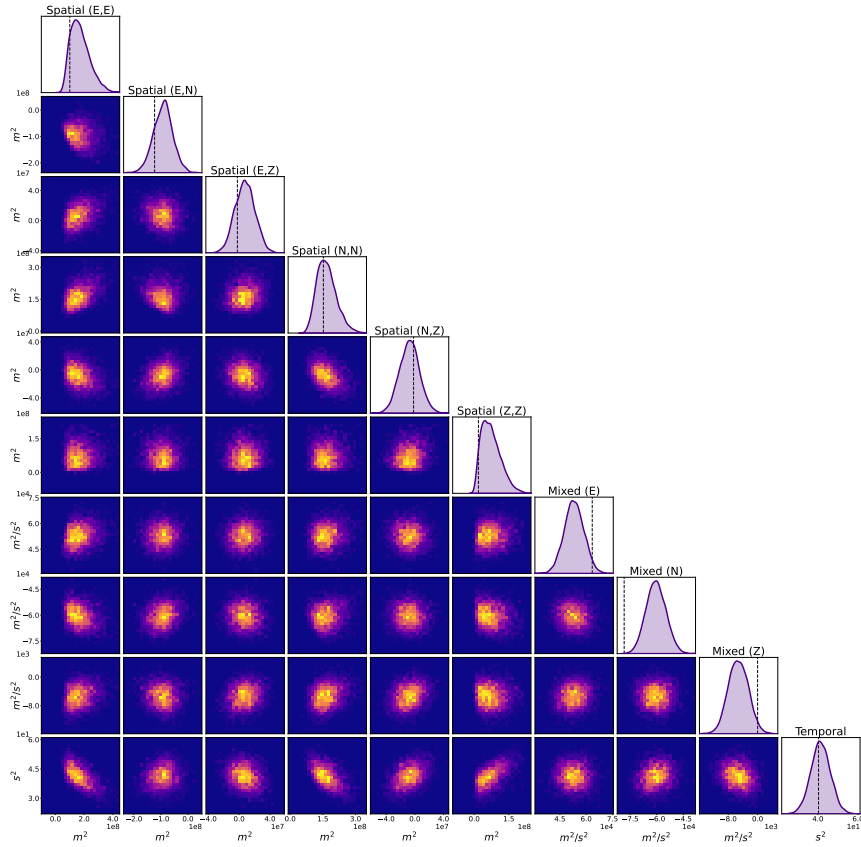


Figure 2. Marginal and joint probability density plots for the 10 independent parameters inverted for the synthetic test in this study. Off-diagonal plots are 2-dimensional histogram plots representing the joint probability distribution for each pair of independent parameters. On-diagonal plots are kernel density estimate plots for the marginal distributions of the adjacent joint probability distributions. Black dotted lines indicated the anticipated solution for each parameter in the inversion.

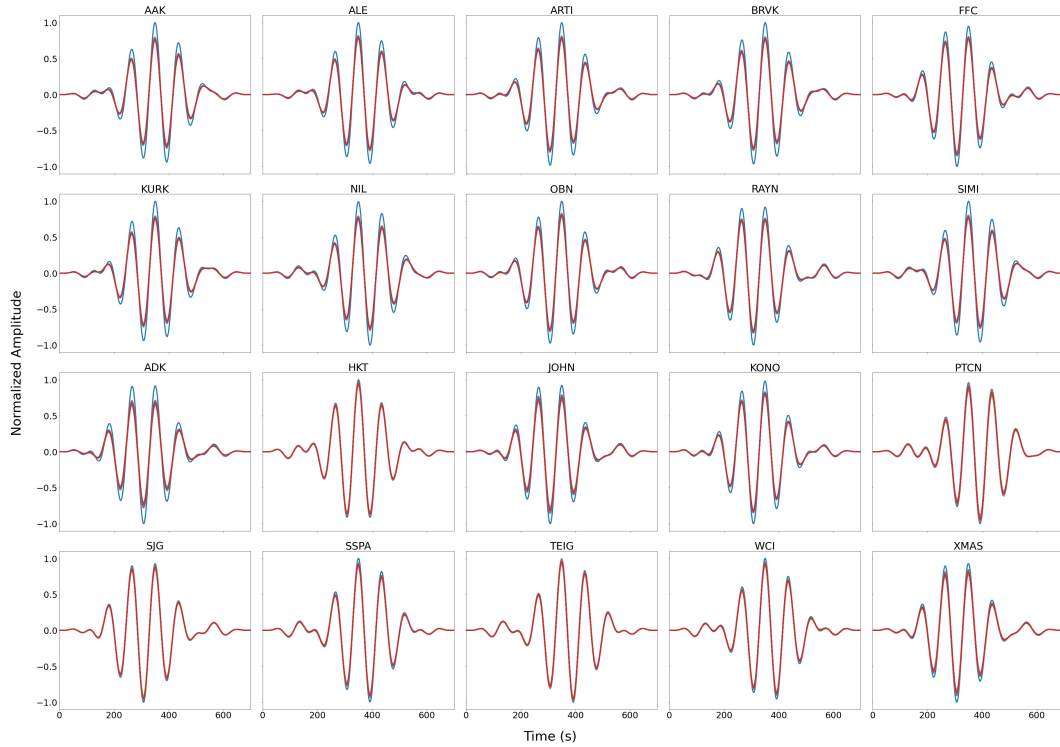


Figure 3. Waveform fits for a large subset of the windowed waveforms for the synthetic test conducted in this study. Waveforms are labeled according to the GSN station at which they were generated. Black waveforms are synthetic observations. Gray waveforms are generated using a single solution from the ensemble of solutions from our inversion. Waveforms from each solution in the ensemble are plotted. Red waveforms are generated using the mean solution of the ensemble of solutions from our inversion. Blue waveforms are generated using only the gCMT solution and exclude any consideration of the second moments of the stress glut.

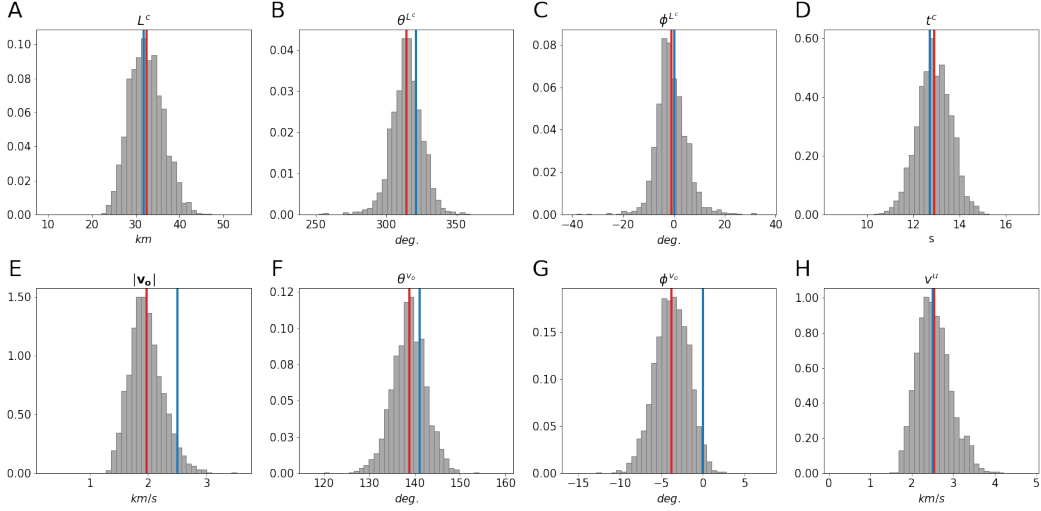


Figure 4. Physically motivated representations of the ensembles of second moment solutions for the synthetic test. A. characteristic length (L^c), B. characteristic length strike (θ^{L^c}), C. characteristic length plunge (ϕ^{L^c}), D. characteristic duration (t^c), E. instantaneous centroid velocity magnitude ($|\mathbf{v}_0|$), F. instantaneous centroid velocity strike ($\theta^{\mathbf{v}_0}$), G. instantaneous centroid velocity plunge ($\phi^{\mathbf{v}_0}$), H. average velocity upper bound (v^u). Histogram shows density of realizations in the ensemble. Red vertical line shows the mean realization. Blue line shows the anticipated realization.

353 respectively. The characteristic duration of the rupture is 14.5 ± 1.1 s. The instantaneous
 354 centroid velocity of the Ridgecrest mainshock has a magnitude of 1.3 ± 0.3 km/s with
 355 strike and plunge of $127.4 \pm 9.9^\circ$ and $1.3 \pm 4.8^\circ$ respectively. Finally, the average velocity
 356 upper bound is 3.3 ± 0.6 km/s. We summarize the results for the spatial and mixed second
 357 moments by plotting projections of ellipsoids defined using $r^c(\hat{\mathbf{n}})$ from equation 3, which
 358 yield descriptions of the volume in which most of the moment of the source was released,
 359 and \mathbf{v}_0 for a subset of 500 solutions from our ensemble of second moment solutions for this
 360 source in Figure 8.

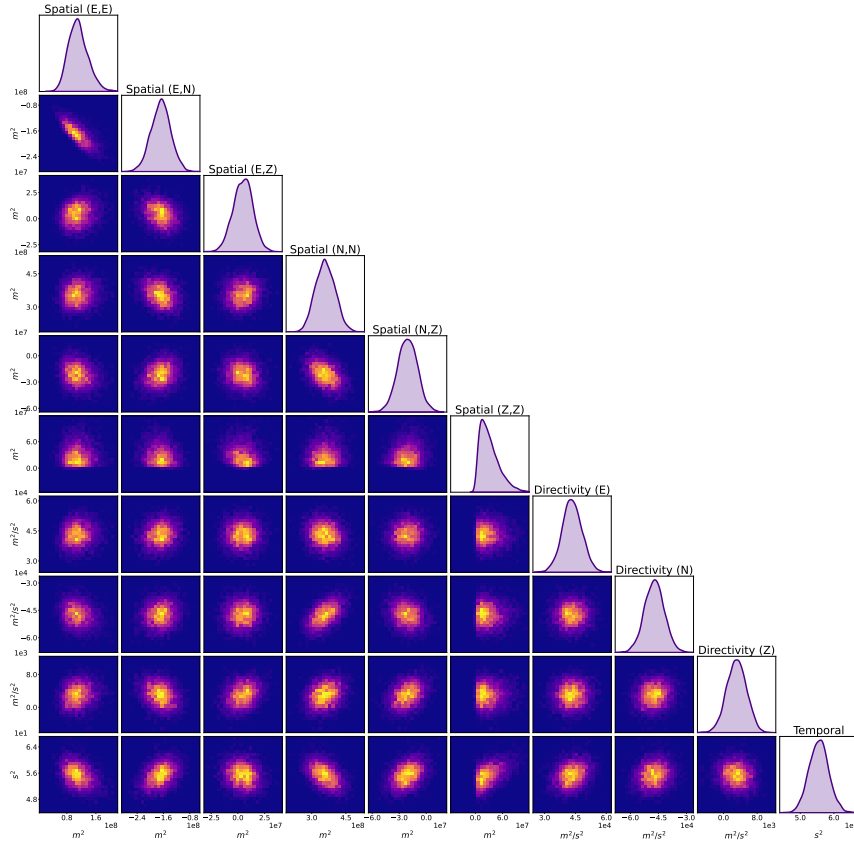


Figure 5. Marginal and joint probability density plots for the 10 independent parameters inverted for in this study. Off-diagonal plots are 2-dimensional histogram plots representing the joint probability distribution for each pair of independent parameters. On-diagonal plots are kernel density estimate plots for the marginal distributions of the adjacent joint probability distributions.

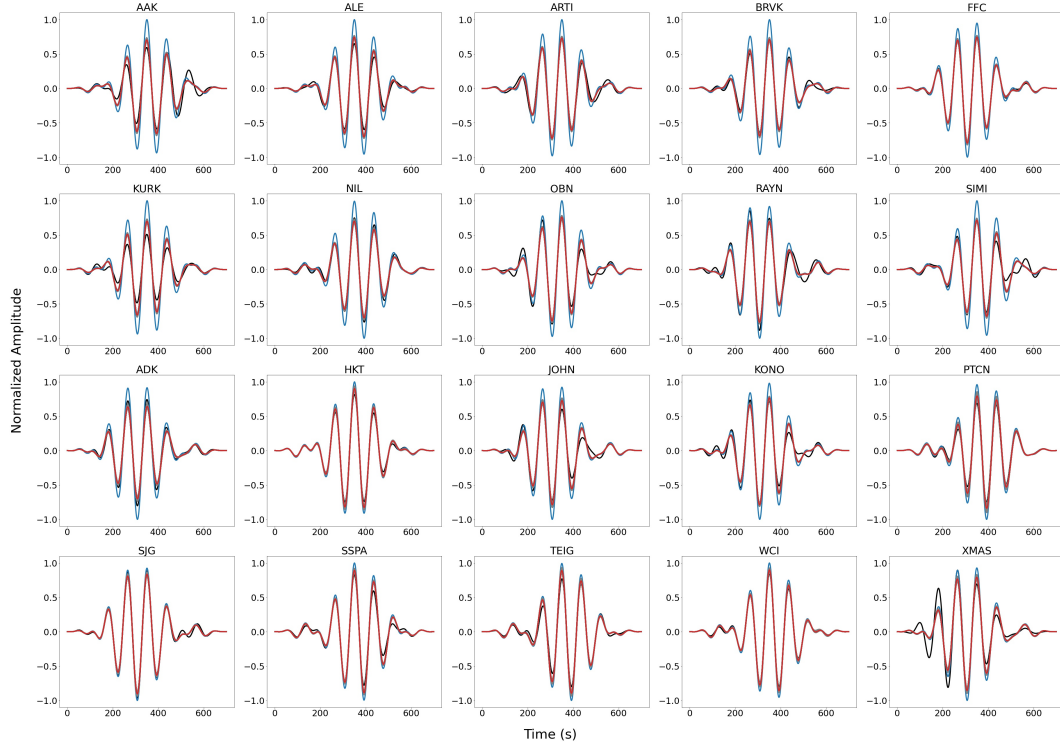


Figure 6. Waveform fits for a subset of the windowed waveforms used in this study. Waveforms are labeled according to the GSN station at which they were recorded. Black waveforms are observations. Gray waveforms are generated using a single solution from the ensemble of solutions from our inversion. Waveforms from each solution in the ensemble are plotted. Red waveforms are generated using the mean solution of the ensemble of solutions from our inversion. Blue waveforms are generated using only the gCMT solution and exclude any consideration of the second moments of the stress glut.

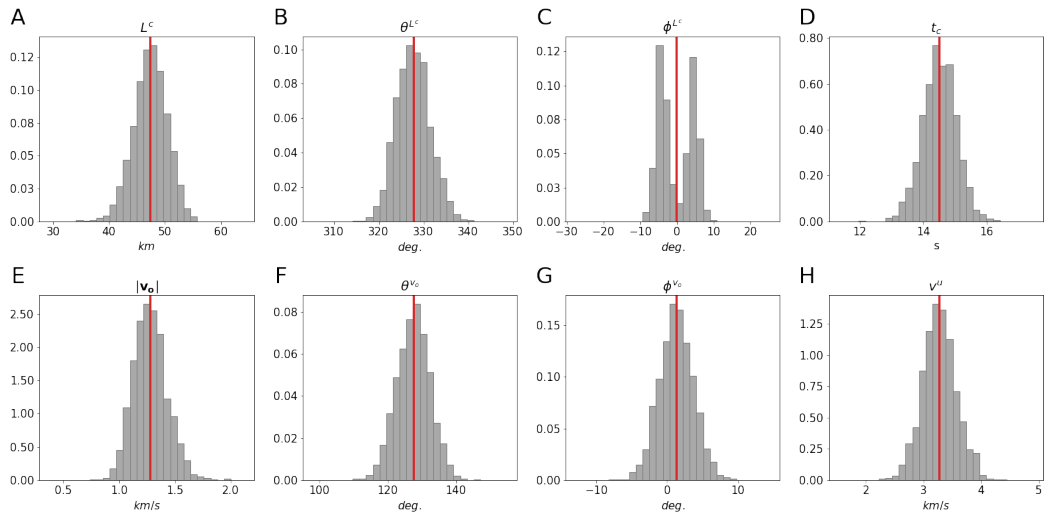


Figure 7. Physically motivated representations of the ensembles of second moment solutions for the 2019 Ridgecrest mainshock. A. characteristic length (L^c), B. characteristic length strike (θ^{L^c}), C. characteristic length plunge (ϕ^{L^c}), D. characteristic duration (t^c), E. instantaneous centroid velocity magnitude ($|\mathbf{v}_0|$), F. instantaneous centroid velocity strike ($\theta^{\mathbf{v}_0}$), G. instantaneous centroid velocity plunge ($\phi^{\mathbf{v}_0}$), H. average velocity upper bound (v^u). Histogram shows density of realizations in the ensemble. Red vertical line shows the mean realization.

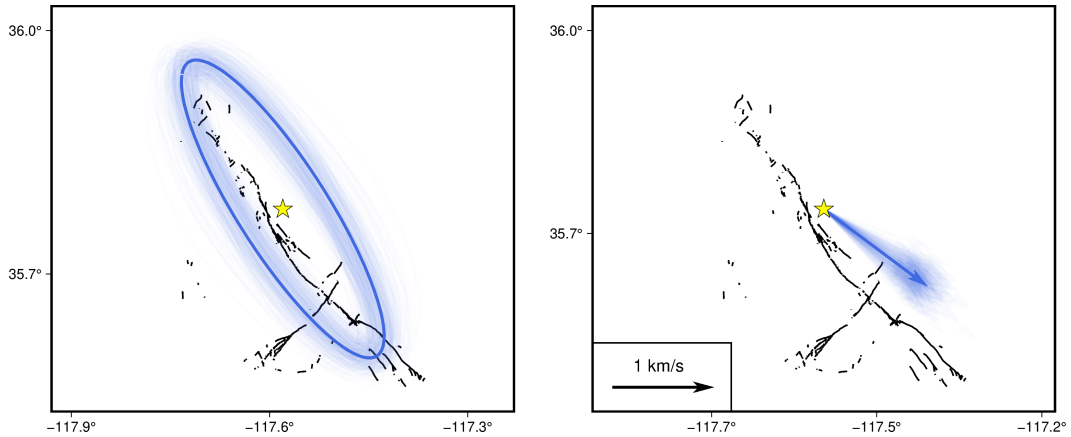


Figure 8. Summary figure of the map-view spatial and directivity features of the 2019 Ridgecrest mainshock as derived from the second moment inversion. Left: Map-view projections of a 500-solution subset of the ensemble of second spatial moment ellipsoids solved for in this study. Ellipsoids are defined using $r_c(\hat{\mathbf{n}})$ in equation 3. Right: Map-view projections of a 500-solution subset of the ensemble of \mathbf{v}_0 , as defined in equation 4, solved for in this study. Black lines represent the surface-rupture faults mapped after the Ridgecrest mainshock. Yellow star marks the location of the gCMT centroid of the Ridgecrest mainshock. Transparent blue lines represent a single solution from the ensemble of second moment solutions. Solid blue lines represent the mean solution from the ensemble second moment solutions.

5 Discussion

When evaluating the solutions described in Figures 4, 7, and 8 and when contextualizing these solutions with previous results, it is important to keep in mind that these quantities are derived parameters from the variance of the stress glut distribution. This is distinct from other types of source parameterizations, such as finite-fault slip distributions, which attempt to solve for an approximation of the full stress glut distribution. Thus, the solutions presented in this study, while physically meaningful, ought to be considered as a separate category of rupture parameterization that should be compared to other rupture parameterizations cautiously. With this in mind, we can begin to assess whether the solutions given in this study yield a reasonable low-dimensional story of the Ridgecrest mainshock rupture.

In general, the ensemble of solutions for the Ridgecrest mainshock is well constrained and largely agrees with what is already known about the event. As is shown in Figure 8, the largest principal axis of the ellipsoid representation is well-aligned with the faults that are known to have ruptured during the mainshock. Additionally, the characteristic length of this rupture is in close agreement with the bulk of estimates of rupture extent for this earthquake. Also shown in Figure 8, the directivity vectors are aligned with these faults and suggest a rupture scenario in which the instantaneous centroid propagates from the NW to the SE. This unilateral behavior is in agreement with other estimates of the directivity of the event. The characteristic durations for this event, which suggest the period of time in which the majority of the moment, but importantly not all of the moment, was released, is also in agreement with other estimates of duration for this earthquake.

The joint probability distributions shown in Figures 2 and 5 suggest that most of the independent parameters of the second moments of the stress glut are weakly correlated. In general, this weak correlation suggests that a perturbation in one parameter will likely have little effect on the values of other parameters. Perhaps most interesting are the weak correlations between the spatial second moments and the mixed second moments and the

387 weak correlations between the spatial second moments and the temporal second moments.
388 These suggest the intuitive conclusion that changing the velocity of the centroid, which
389 is related to the velocity of rupture, changes the volume that can be ruptured in a given
390 amount of time, and changing the amount of time available for rupture changes the volume
391 through which a rupture of fixed velocity can propagate.

392 The low dimensional second moment estimate of the 2019 Ridgecrest mainshock il-
393 lustrates the unique potential of this methodology for producing probabilistic estimates of
394 finite source properties with few a priori assumptions on the fault geometry and rupture
395 dynamics. The only requirement is a centroid moment tensor solution, which fits nicely into
396 this framework, as the zeroth and first moments represent the scalar moment and centroid
397 position of the earthquake respectively. In fact, the centroid moment tensor solution may
398 be solved concurrently with the second moment solution (McGuire et al., 2000), but this in-
399 troduces nonlinearity and significant additional computational/numerical complexity, which
400 we reserve for future studies. The only constraint required in the inversion is that the source
401 be non-negative in extent, which does not exclude any possible source scenarios. However,
402 it is indeed easy to impose additional constraints on the second moments through the use of
403 informed priors on the inversion parameters. Such informed priors should be imposed with
404 the understanding that the second moments describe a covariance matrix of a 4-dimensional
405 stress glut distribution. That is, informed priors are not necessarily being placed on the
406 possible source dimensions, but instead are being placed on the possible covariances of the
407 source distribution.

408 The 2019 Ridgecrest mainshock is a well-studied event, and many of the features of
409 the rupture that are illuminated by this inversion were already known. However, this study
410 serves as an illustration of some key strengths of this technique. Firstly, this methodology
411 provides an estimate of the full posterior distribution of these solutions. So, claims regarding
412 rupture finiteness can be made in the context of the full range of possible solutions given the
413 uncertainty in the problem. Having a posterior distribution thus allows us to apply some
414 degree of confidence to specific claims about an earthquake rupture. Consequently, with
415 this methodology, we can make probabilistically supported assessments of the significance
416 of similarities and differences between solutions for different events. Another benefit of this
417 approach is that, given a prescribed correlation structure in the data, the data covariance
418 matrix is solved for as a hyperparameter in the inversion. This means that the uncertainty
419 of the posterior is reflective of data uncertainty that is solved for dynamically according to
420 the structure of the data and the model.

421 Additionally, this methodology requires few of the a priori assumptions that present
422 challenges and inaccuracies in other source finiteness estimation techniques, like finite-fault
423 slip distributions. For example, this inversion technique does not require any prior character-
424 ization of the fault surface. Although the fault surface for Ridgecrest is well-approximated,
425 for many global events, like offshore earthquakes, determining a fault surface is challenging,
426 and so this methodology presents a substantial advantage for these events. Indeed, this
427 methodology does not even require that all of the slip take place on a surface, but instead
428 allows for moment release in a volume. This is apparent in Figure 8, where the spatial second
429 moment is represented as an ellipsoid with significant width orthogonal to the major axis
430 of the ellipsoid. Indeed, with this methodology, scientifically interesting properties like the
431 fault-normal width of rupture can be probabilistically constrained and compared between
432 events.

433 Another strength of this methodology is implicit in the fact that we employed this
434 methodology using only GSN teleseismic data. Although the Ridgecrest earthquake occurred
435 in an exceptionally well-instrumented area, for many global events teleseismic data is the
436 only available information for characterizing the coseismic rupture. Thus for numerous
437 events, given this limitation in data availability, robust information concerning rupture
438 finiteness is scarce. This methodology then serves as a potentially pivotal tool in discerning
439 probabilistic characterizations of earthquakes globally. Relatedly, large global events occur

440 infrequently, and thus historic events are a crucial component in our understanding of large
441 earthquakes. The continuity of teleseismic data collection by the GSN for over two decades
442 thus allows for this methodology to be readily applied to a large number of previous global
443 earthquakes.

444

6 Conclusions

445

446

447

448

449

450

451

452

453

454

455

456

457

458

459

In this study, we develop a Bayesian framework for computing second moments of the stress glut of earthquakes using teleseismic data. This framework incorporates a positive-definite constraint under Cholesky decomposition and employs Hamiltonian Monte Carlo sampling to efficiently probe the parameter space. This methodology provides robust estimates of uncertainty by sampling the posterior distribution of solutions with dynamic error computation and accounting for the temporal correlation structure in the waveform data. These second moments of the stress glut provide a low-dimensional, physically-motivated representation of source volume, directivity, and duration that requires no *a priori* assumptions and is repeatable and comparable between events. We verify this methodology using a synthetic test and apply this framework to the 2019 Ridgecrest Sequence mainshock. We show that our solutions for this event yield event parameters that largely agree with what is known about this event and includes an estimate of the full posterior distribution. Our solution also illustrates some key strengths of this rupture-parameterization, namely the independence of this solution from a prescribed fault surface and the reliance of this inversion on only teleseismic data.

Acknowledgments

This work was partially funded by the National Science Foundation's (NSF) Graduate Research Fellowships Program (GRFP) under grant number DGE-1745301. The teleseismic waveforms used in this study are from the Global Seismographic Network (GSN) operated by Scripps Institution of Oceanography (II: IRIS/IDA; <https://doi.org/10.7914/SN/II>) (Scripps Institution Of Oceanography, 1986) and the Albuquerque Seismological Laboratory (IU: IRIS/USGS; <https://doi.org/10.7914/SN/IU>) (Albuquerque Seismological Laboratory (ASL)/USGS, 1988). These waveforms and associated metadata used in this study were accessed through the IRIS Data Management Center (DMC). The centroid and moment tensor solution used in this study were obtained from Global Centroid Moment Tensor (gCMT) catalog (Dziewonski et al., 1981; Ekström et al., 2012) at <https://www.globalcmt.org/>. The synthetic waveforms used in this study were generated using the software Salvus, (Afanasiev et al., 2019), available at <https://mondaic.com/>. Figure 1 was generated using The Generic Mapping Tools (GMT), version 6 (Wessel et al., 2019), available at <https://www.generic-mapping-tools.org/>. We would like to thank Dr. Hiroo Kanamori for sharing his experience and providing perceptive comments. We would also like to thank two anonymous reviewers for their insightful comments which greatly improved this manuscript, and the editor Dr. Rachel Abercrombie for facilitating the review process.

References

- Afanasiev, M., Boehm, C., van Driel, M., Krischer, L., Rietmann, M., May, D. A., ... Fichtner, A. (2019). Modular and flexible spectral-element waveform modelling in two and three dimensions. *Geophysical Journal International*, *216*(3), 1675-1692. doi: 10.1093/gji/ggy469
- Albuquerque Seismological Laboratory (ASL)/USGS. (1988). *Global Seismograph Network (GSN - IRIS/USGS)*. International Federation of Digital Seismograph Networks. Retrieved from <http://www.fdsn.org/doi/10.7914/SN/IU> doi: 10.7914/SN/IU
- Ammon, C. J. (2005, May). Rupture process of the 2004 Sumatra-Andaman Earthquake. *Science*, *308*(5725), 1133-1139. Retrieved 2021-06-21, from <https://www.sciencemag.org/lookup/doi/10.1126/science.1112260> doi: 10.1126/science.1112260
- Backus, G., & Mulcahy, M. (1976a, August). Moment tensors and other phenomenological descriptions of seismic sources—I. Continuous displacements. *Geophysical Journal International*, *46*(2), 341-361. Retrieved 2020-11-05, from <https://academic.oup.com/gji/article-lookup/doi/10.1111/j.1365-246X.1976.tb04162.x> doi: 10.1111/j.1365-246X.1976.tb04162.x
- Backus, G., & Mulcahy, M. (1976b, November). Moment tensors and other phenomenological descriptions of seismic sources—II. Discontinuous displacements. *Geophysical Journal International*, *47*(2), 301-329. Retrieved 2020-11-05, from <https://academic.oup.com/gji/article-lookup/doi/10.1111/j.1365-246X.1976.tb01275.x> doi: 10.1111/j.1365-246X.1976.tb01275.x
- Backus, G. E. (1977, October). Interpreting the seismic glut moments of total degree two or less. *Geophysical Journal International*, *51*(1), 1-25. Retrieved 2020-11-05, from <https://academic.oup.com/gji/article-lookup/doi/10.1111/j.1365-246X.1977.tb04187.x> doi: 10.1111/j.1365-246X.1977.tb04187.x
- Barnhart, W. D., Hayes, G. P., & Gold, R. D. (2019, November). The July 2019 Ridgecrest, California, Earthquake Sequence: Kinematics of Slip and Stressing in Cross-Fault Ruptures. *Geophysical Research Letters*, *46*(21), 11859-11867. Retrieved 2021-11-09, from <https://onlinelibrary.wiley.com/doi/10.1029/2019GL084741> doi: 10.1029/2019GL084741
- Bukchin, B. (1995, August). Determination of stress glut moments of total degree 2 from teleseismic surface wave amplitude spectra. *Tectonophysics*, *248*(3-4), 185-191. Retrieved 2020-11-05, from <https://linkinghub.elsevier.com/retrieve/pii/004019519400271A> doi: 10.1016/0040-1951(94)00271-A
- Chen, P. (2005, June). Finite-moment tensor of the 3 September 2002 Yorba Linda Earth-

- 513 quake. *Bulletin of the Seismological Society of America*, 95(3), 1170–1180. Re-
 514 trieved 2020-11-05, from [https://pubs.geoscienceworld.org/bssa/article/95/](https://pubs.geoscienceworld.org/bssa/article/95/3/1170-1180/103154)
 515 [3/1170-1180/103154](https://pubs.geoscienceworld.org/bssa/article/95/3/1170-1180/103154) doi: 10.1785/0120040094
- 516 Dahlen, F., & Tromp, J. (1998). *Theoretical global seismology*. Princeton, N.J.: Princeton
 517 University Press.
- 518 Du, Y., Aydin, A., & Segall, P. (1992, August). Comparison of various inversion techniques
 519 as applied to the determination of a geophysical deformation model for the 1983 Borah
 520 Peak Earthquake. *Bulletin of the Seismological Society of America*, 82(4), 1840–1866.
- 521 Duputel, Z., Agram, P. S., Simons, M., Minson, S. E., & Beck, J. L. (2014,
 522 April). Accounting for prediction uncertainty when inferring subsurface fault
 523 slip. *Geophysical Journal International*, 197(1), 464–482. Retrieved 2020-11-
 524 03, from [http://academic.oup.com/gji/article/197/1/464/686313/Accounting](http://academic.oup.com/gji/article/197/1/464/686313/Accounting-for-prediction-uncertainty-when)
 525 [-for-prediction-uncertainty-when](http://academic.oup.com/gji/article/197/1/464/686313/Accounting-for-prediction-uncertainty-when) doi: 10.1093/gji/ggt517
- 526 DuRoss, C. B., Gold, R. D., Dawson, T. E., Scharer, K. M., Kendrick, K. J., Ak-
 527 ciz, S. O., ... Zinke, R. (2020, August). Surface Displacement Distribu-
 528 tions for the July 2019 Ridgecrest, California, Earthquake Ruptures. *Bulletin*
 529 *of the Seismological Society of America*, 110(4), 1400–1418. Retrieved 2021-
 530 11-09, from [https://pubs.geoscienceworld.org/ssa/bssa/article/110/4/1400/](https://pubs.geoscienceworld.org/ssa/bssa/article/110/4/1400/587507/Surface-Displacement-Distributions-for-the-July)
 531 [587507/Surface-Displacement-Distributions-for-the-July](https://pubs.geoscienceworld.org/ssa/bssa/article/110/4/1400/587507/Surface-Displacement-Distributions-for-the-July) doi: 10.1785/
 532 0120200058
- 533 Dziewonski, A. M., Chou, T. A., & Woodhouse, J. H. (1981, April). Determination of
 534 earthquake source parameters from waveform data for studies of global and regional
 535 seismicity. *Journal of Geophysical Research: Solid Earth*, 86(B4), 2825–2852. Re-
 536 trieved 2020-11-05, from <http://doi.wiley.com/10.1029/JB086iB04p02825> doi:
 537 10.1029/JB086iB04p02825
- 538 Ekström, G., Nettles, M., & Dziewoński, A. (2012, June). The global CMT project
 539 2004–2010: Centroid-moment tensors for 13,017 earthquakes. *Physics of the Earth and*
 540 *Planetary Interiors*, 200-201, 1–9. Retrieved 2020-11-05, from [https://linkinghub](https://linkinghub.elsevier.com/retrieve/pii/S0031920112000696)
 541 [.elsevier.com/retrieve/pii/S0031920112000696](https://linkinghub.elsevier.com/retrieve/pii/S0031920112000696) doi: 10.1016/j.pepi.2012.04
 542 .002
- 543 GCMT. (2019). *Mw 7.0 central california*. Retrieved from [https://www.globalcmt.org/](https://www.globalcmt.org/cgi-bin/globalcmt-cgi-bin/CMT5/form?itype=ynd&yr=2019&mo=07&day=1&otype=ynd&oyr=2019&omo=07&oday=10&jyr=1976&jday=1&ojyr=1976&ojday=1&nday=1&lmw=7&umw=10&lms=0&ums=10&lmb=0&umb=10&llat=-90&ulat=90&llon=-180&ulon=180&lhd=0&uhd=1000<s=-9999&uts=9999&lpe1=0&upe1=90&lpe2=0&upe2=90&list=0)
 544 [cgi-bin/globalcmt-cgi-bin/CMT5/form?itype=ynd&yr=2019&mo=07&day=](https://www.globalcmt.org/cgi-bin/globalcmt-cgi-bin/CMT5/form?itype=ynd&yr=2019&mo=07&day=1&otype=ynd&oyr=2019&omo=07&oday=10&jyr=1976&jday=1&ojyr=1976&ojday=1&nday=1&lmw=7&umw=10&lms=0&ums=10&lmb=0&umb=10&llat=-90&ulat=90&llon=-180&ulon=180&lhd=0&uhd=1000<s=-9999&uts=9999&lpe1=0&upe1=90&lpe2=0&upe2=90&list=0)
 545 [1&otype=ynd&oyr=2019&omo=07&oday=10&jyr=1976&jday=1&ojyr=1976&ojday=](https://www.globalcmt.org/cgi-bin/globalcmt-cgi-bin/CMT5/form?itype=ynd&yr=2019&mo=07&day=1&otype=ynd&oyr=2019&omo=07&oday=10&jyr=1976&jday=1&ojyr=1976&ojday=1&nday=1&lmw=7&umw=10&lms=0&ums=10&lmb=0&umb=10&llat=-90&ulat=90&llon=-180&ulon=180&lhd=0&uhd=1000<s=-9999&uts=9999&lpe1=0&upe1=90&lpe2=0&upe2=90&list=0)
 546 [1&nday=1&lmw=7&umw=10&lms=0&ums=10&lmb=0&umb=10&llat=-90&ulat=90&llon=](https://www.globalcmt.org/cgi-bin/globalcmt-cgi-bin/CMT5/form?itype=ynd&yr=2019&mo=07&day=1&otype=ynd&oyr=2019&omo=07&oday=10&jyr=1976&jday=1&ojyr=1976&ojday=1&nday=1&lmw=7&umw=10&lms=0&ums=10&lmb=0&umb=10&llat=-90&ulat=90&llon=-180&ulon=180&lhd=0&uhd=1000<s=-9999&uts=9999&lpe1=0&upe1=90&lpe2=0&upe2=90&list=0)
 547 [-180&ulon=180&lhd=0&uhd=1000<s=-9999&uts=9999&lpe1=0&upe1=90&lpe2=](https://www.globalcmt.org/cgi-bin/globalcmt-cgi-bin/CMT5/form?itype=ynd&yr=2019&mo=07&day=1&otype=ynd&oyr=2019&omo=07&oday=10&jyr=1976&jday=1&ojyr=1976&ojday=1&nday=1&lmw=7&umw=10&lms=0&ums=10&lmb=0&umb=10&llat=-90&ulat=90&llon=-180&ulon=180&lhd=0&uhd=1000<s=-9999&uts=9999&lpe1=0&upe1=90&lpe2=0&upe2=90&list=0)
 548 [0&upe2=90&list=0](https://www.globalcmt.org/cgi-bin/globalcmt-cgi-bin/CMT5/form?itype=ynd&yr=2019&mo=07&day=1&otype=ynd&oyr=2019&omo=07&oday=10&jyr=1976&jday=1&ojyr=1976&ojday=1&nday=1&lmw=7&umw=10&lms=0&ums=10&lmb=0&umb=10&llat=-90&ulat=90&llon=-180&ulon=180&lhd=0&uhd=1000<s=-9999&uts=9999&lpe1=0&upe1=90&lpe2=0&upe2=90&list=0)
- 549 Gelman, A., Carlin, J., Stern, H., Dunson, D., Vehtari, A., & Rubin, D. (2010). *Bayesian*
 550 *data analysis*. Boca Raton, F.L.: Chapman and Hall-CRC Press.
- 551 Gelman, A., & Rubin, D. (1992). Inference from iterative simulation using multiple se-
 552 quences. *Statistical Science*, 7(4), 457–511.
- 553 Goldberg, D. E., Melgar, D., Sahakian, V. J., Thomas, A. M., Xu, X., Crowell, B. W.,
 554 & Geng, J. (2020, February). Complex Rupture of an Immature Fault Zone: A
 555 Simultaneous Kinematic Model of the 2019 Ridgecrest, CA Earthquakes. *Geophysical*
 556 *Research Letters*, 47(3). Retrieved 2021-11-09, from [https://onlinelibrary.wiley](https://onlinelibrary.wiley.com/doi/10.1029/2019GL086382)
 557 [.com/doi/10.1029/2019GL086382](https://onlinelibrary.wiley.com/doi/10.1029/2019GL086382) doi: 10.1029/2019GL086382
- 558 Hartzell, S. H., & Heaton, T. H. (1983, December). Inversion of strong ground motion and
 559 teleseismic waveform data for the fault rupture history of the 1979 Imperial Valley,
 560 California Earthquake. *Bulletin of the Seismological Society of America*, 73(6), 1553–
 561 1583.
- 562 Ide, S., Baltay, A., & Beroza, G. C. (2011, June). Shallow Dynamic Overshoot and Energetic
 563 Deep Rupture in the 2011 Mw 9.0 Tohoku-Oki Earthquake. *Science*, 332(6036),
 564 1426–1429. Retrieved 2021-06-21, from [https://www.sciencemag.org/lookup/doi/](https://www.sciencemag.org/lookup/doi/10.1126/science.1207020)
 565 [10.1126/science.1207020](https://www.sciencemag.org/lookup/doi/10.1126/science.1207020) doi: 10.1126/science.1207020
- 566 Innes, M. (2019, March). Don’t Unroll Adjoint: Differentiating SSA-Form Programs.
 567 *arXiv:1810.07951 [cs]*. Retrieved 2021-06-29, from <http://arxiv.org/abs/1810>

- 568 .07951 (arXiv: 1810.07951)
- 569 Jia, Z., Wang, X., & Zhan, Z. (2020, September). Multifault Models of the 2019 Ridgecrest
570 Sequence Highlight Complementary Slip and Fault Junction Instability. *Geophysical*
571 *Research Letters*, *47*(17). Retrieved 2021-11-09, from [https://onlinelibrary.wiley](https://onlinelibrary.wiley.com/doi/10.1029/2020GL089802)
572 [.com/doi/10.1029/2020GL089802](https://onlinelibrary.wiley.com/doi/10.1029/2020GL089802) doi: 10.1029/2020GL089802
- 573 Jin, Z., & Fialko, Y. (2020, August). Finite Slip Models of the 2019 Ridgecrest Earth-
574 quake Sequence Constrained by Space Geodetic Data and Aftershock Locations. *Bul-*
575 *letin of the Seismological Society of America*, *110*(4), 1660–1679. Retrieved 2021-
576 11-09, from [https://pubs.geoscienceworld.org/ssa/bssa/article/110/4/1660/](https://pubs.geoscienceworld.org/ssa/bssa/article/110/4/1660/587725/Finite-Slip-Models-of-the-2019-Ridgecrest)
577 [587725/Finite-Slip-Models-of-the-2019-Ridgecrest](https://pubs.geoscienceworld.org/ssa/bssa/article/110/4/1660/587725/Finite-Slip-Models-of-the-2019-Ridgecrest) doi: 10.1785/0120200060
- 578 Lay, T. (2018, May). A review of the rupture characteristics of the 2011 Tohoku-
579 oki Mw 9.1 earthquake. *Tectonophysics*, *733*, 4–36. Retrieved 2021-06-21, from
580 <https://linkinghub.elsevier.com/retrieve/pii/S0040195117303992> doi: 10
581 [.1016/j.tecto.2017.09.022](https://linkinghub.elsevier.com/retrieve/pii/S0040195117303992)
- 582 Lee, E.-J., Chen, P., Jordan, T. H., & Wang, L. (2011, July). Rapid full-wave centroid mo-
583 ment tensor (CMT) inversion in a three-dimensional earth structure model for earth-
584 quakes in Southern California: Rapid full-wave CMT inversion. *Geophysical Jour-*
585 *nal International*, *186*(1), 311–330. Retrieved 2021-06-21, from [https://academic](https://academic.oup.com/gji/article-lookup/doi/10.1111/j.1365-246X.2011.05031.x)
586 [.oup.com/gji/article-lookup/doi/10.1111/j.1365-246X.2011.05031.x](https://academic.oup.com/gji/article-lookup/doi/10.1111/j.1365-246X.2011.05031.x) doi: 10
587 [.1111/j.1365-246X.2011.05031.x](https://academic.oup.com/gji/article-lookup/doi/10.1111/j.1365-246X.2011.05031.x)
- 588 Liu, C., Lay, T., Brodsky, E. E., Dascher-Cousineau, K., & Xiong, X. (2019, November).
589 Coseismic Rupture Process of the Large 2019 Ridgecrest Earthquakes From Joint
590 Inversion of Geodetic and Seismological Observations. *Geophysical Research Letters*,
591 *46*(21), 11820–11829. Retrieved 2021-11-09, from [https://onlinelibrary.wiley](https://onlinelibrary.wiley.com/doi/10.1029/2019GL084949)
592 [.com/doi/10.1029/2019GL084949](https://onlinelibrary.wiley.com/doi/10.1029/2019GL084949) doi: 10.1029/2019GL084949
- 593 McGuire, J. J. (2002, December). Predominance of Unilateral Rupture for a Global Cat-
594 alog of Large Earthquakes. *Bulletin of the Seismological Society of America*, *92*(8),
595 3309–3317. Retrieved 2020-11-05, from [https://pubs.geoscienceworld.org/bssa/](https://pubs.geoscienceworld.org/bssa/article/92/8/3309-3317/103071)
596 [article/92/8/3309-3317/103071](https://pubs.geoscienceworld.org/bssa/article/92/8/3309-3317/103071) doi: 10.1785/0120010293
- 597 McGuire, J. J. (2004, April). Estimating Finite Source Properties of Small Earthquake
598 Ruptures. *Bulletin of the Seismological Society of America*, *94*(2), 377–393. Re-
599 trieved 2020-11-05, from [https://pubs.geoscienceworld.org/bssa/article/94/](https://pubs.geoscienceworld.org/bssa/article/94/2/377-393/146918)
600 [2/377-393/146918](https://pubs.geoscienceworld.org/bssa/article/94/2/377-393/146918) doi: 10.1785/0120030091
- 601 McGuire, J. J., Zhao, L., & Jordan, T. H. (2000, August). Rupture dimensions of the
602 1998 Antarctic Earthquake from low-frequency waves. *Geophysical Research Letters*,
603 *27*(15), 2305–2308. Retrieved 2020-11-05, from [http://doi.wiley.com/10.1029/](http://doi.wiley.com/10.1029/1999GL011186)
604 [1999GL011186](http://doi.wiley.com/10.1029/1999GL011186) doi: 10.1029/1999GL011186
- 605 McGuire, J. J., Zhao, L., & Jordan, T. H. (2001, June). Teleseismic inversion for the second-
606 degree moments of earthquake space-time distributions. *Geophysical Journal Interna-*
607 *tional*, *145*(3), 661–678. Retrieved 2020-11-05, from [https://academic.oup.com/](https://academic.oup.com/gji/article-lookup/doi/10.1046/j.1365-246x.2001.01414.x)
608 [gji/article-lookup/doi/10.1046/j.1365-246x.2001.01414.x](https://academic.oup.com/gji/article-lookup/doi/10.1046/j.1365-246x.2001.01414.x) doi: 10.1046/
609 [j.1365-246x.2001.01414.x](https://academic.oup.com/gji/article-lookup/doi/10.1046/j.1365-246x.2001.01414.x)
- 610 Meng, H., McGuire, J. J., & Ben-Zion, Y. (2020, April). Semiautomated estimates of
611 directivity and related source properties of small to moderate Southern California
612 earthquakes using second seismic moments. *Journal of Geophysical Research: Solid*
613 *Earth*, *125*(4), e2019JB018566. Retrieved 2021-06-23, from [https://onlinelibrary](https://onlinelibrary.wiley.com/doi/10.1029/2019JB018566)
614 [.wiley.com/doi/10.1029/2019JB018566](https://onlinelibrary.wiley.com/doi/10.1029/2019JB018566) doi: 10.1029/2019JB018566
- 615 Minson, S. E., Simons, M., & Beck, J. L. (2013, September). Bayesian in-
616 version for finite fault earthquake source models I—theory and algorithm.
617 *Geophysical Journal International*, *194*(3), 1701–1726. Retrieved 2020-11-
618 03, from [http://academic.oup.com/gji/article/194/3/1701/645931/Bayesian](http://academic.oup.com/gji/article/194/3/1701/645931/Bayesian-inversion-for-finite-fault-earthquake)
619 [-inversion-for-finite-fault-earthquake](http://academic.oup.com/gji/article/194/3/1701/645931/Bayesian-inversion-for-finite-fault-earthquake) doi: 10.1093/gji/ggt180
- 620 Monelli, D., Mai, P. M., Jónsson, S., & Giardini, D. (2009, January). Bayesian imag-
621 ing of the 2000 Western Tottori (Japan) earthquake through fitting of strong mo-
622 tion and GPS data. *Geophysical Journal International*, *176*(1), 135–150. Retrieved

- 2021-06-21, from <https://academic.oup.com/gji/article-lookup/doi/10.1111/j.1365-246X.2008.03943.x> doi: 10.1111/j.1365-246X.2008.03943.x
- Moreno, M., Rosenau, M., & Oncken, O. (2010, September). 2010 Maule earthquake slip correlates with pre-seismic locking of Andean subduction zone. *Nature*, *467*(7312), 198–202. Retrieved 2021-06-21, from <http://www.nature.com/articles/nature09349> doi: 10.1038/nature09349
- Moulik, P., & Ekström, G. (2014, December). An anisotropic shear velocity model of the Earth’s mantle using normal modes, body waves, surface waves and long-period waveforms. *Geophysical Journal International*, *199*(3), 1713–1738. Retrieved 2021-11-04, from <http://academic.oup.com/gji/article/199/3/1713/617840/An-anisotropic-shear-velocity-model-of-the-Earths> doi: 10.1093/gji/ggu356
- Neal, R. (2010). *MCMC using Hamiltonian Dynamics*. Boca Raton, F.L.: Chapman and Hall-CRC Press.
- Ponti, D. J., Blair, J. L., Rosa, C. M., Thomas, K., Pickering, A. J., Akciz, S., . . . Zinke, R. (2020, September). Documentation of Surface Fault Rupture and Ground-Deformation Features Produced by the 4 and 5 July 2019 Mw 6.4 and Mw 7.1 Ridgecrest Earthquake Sequence. *Seismological Research Letters*, *91*(5), 2942–2959. Retrieved 2021-11-09, from <https://pubs.geoscienceworld.org/ssa/srl/article/91/5/2942/588337/Documentation-of-Surface-Fault-Rupture-and> doi: 10.1785/0220190322
- Ross, Z. E., Idini, B., Jia, Z., Stephenson, O. L., Zhong, M., Wang, X., . . . Jung, J. (2019, October). Hierarchical interlocked orthogonal faulting in the 2019 Ridgecrest earthquake sequence. *Science*, *366*(6463), 346–351. Retrieved 2021-11-09, from <https://www.science.org/doi/10.1126/science.aaz0109> doi: 10.1126/science.aaz0109
- Saito, T., Ito, Y., Inazu, D., & Hino, R. (2011, April). Tsunami source of the 2011 Tohoku-Oki earthquake, Japan: Inversion analysis based on dispersive tsunami simulations. *Geophysical Research Letters*, *38*(7), L00G19. Retrieved 2021-06-21, from <http://doi.wiley.com/10.1029/2011GL049089> doi: 10.1029/2011GL049089
- Scripps Institution Of Oceanography. (1986). *IRIS/IDA Seismic Network*. International Federation of Digital Seismograph Networks. Retrieved from <http://www.fdsn.org/doi/10.7914/SN/II> doi: 10.7914/SN/II
- Silver, P. G., & Jordan, T. H. (1983). Total-moment spectra of fourteen large earthquakes. *Journal of Geophysical Research*, *88*(B4), 3273. Retrieved 2020-11-05, from <http://doi.wiley.com/10.1029/JB088iB04p03273> doi: 10.1029/JB088iB04p03273
- Tarantola, A. (2005). *Inverse Problem Theory and Methods for Model Parameter Estimation*. Society for Industrial and Applied Mathematics. Retrieved 2020-11-03, from <http://epubs.siam.org/doi/book/10.1137/1.9780898717921> doi: 10.1137/1.9780898717921
- USGS. (2019). *M 7.1 - 2019 ridgecrest earthquake sequence*. Retrieved from https://earthquake.usgs.gov/earthquakes/eventpage/ci38457511/moment-tensor?source=us&code=us_70004bn0_mw
- USGS, & CGS. (2021). *Quaternary fault and fold database for the united states*. Retrieved from <https://www.usgs.gov/natural-hazards/earthquake-hazards/faults>
- Vallée, M., & Douet, V. (2016, August). A new database of source time functions (STFs) extracted from the SCARDEC method. *Physics of the Earth and Planetary Interiors*, *257*, 149–157. Retrieved 2020-11-03, from <https://linkinghub.elsevier.com/retrieve/pii/S0031920116300735> doi: 10.1016/j.pepi.2016.05.012
- Wald, D. J., & Heaton, T. H. (1992). Spatial and temporal distribution of slip for the 1992 Landers, California, Earthquake. *Bulletin of the Seismological Society of America*, *84*(3), 668–691.
- Walsh, D., Arnold, R., & Townend, J. (2009, January). A Bayesian approach to determining and parametrizing earthquake focal mechanisms. *Geophysical Journal International*, *176*(1), 235–255. Retrieved 2021-06-21, from <https://academic.oup.com/gji/article-lookup/doi/10.1111/j.1365-246X.2008.03979.x> doi: 10.1111/j.1365-246X.2008.03979.x
- Wang, K., Dreger, D. S., Tinti, E., Bürgmann, R., & Taira, T. (2020, Au-

- 678 gust). Rupture Process of the 2019 Ridgecrest, California Mw 6.4 Foreshock
679 and Mw 7.1 Earthquake Constrained by Seismic and Geodetic Data. *Bulletin*
680 *of the Seismological Society of America*, 110(4), 1603–1626. Retrieved 2021-
681 11-09, from [https://pubs.geoscienceworld.org/ssa/bssa/article/110/4/1603/](https://pubs.geoscienceworld.org/ssa/bssa/article/110/4/1603/587915/Rupture-Process-of-the-2019-Ridgecrest-California)
682 [587915/Rupture-Process-of-the-2019-Ridgecrest-California](https://pubs.geoscienceworld.org/ssa/bssa/article/110/4/1603/587915/Rupture-Process-of-the-2019-Ridgecrest-California) doi: 10.1785/
683 0120200108
- 684 Wessel, P., Luis, J. F., Uieda, L., Scharroo, R., Wobbe, F., Smith, W. H. F., & Tian, D.
685 (2019). *The generic mapping tools*. Retrieved from [https://www.generic-mapping](https://www.generic-mapping-tools.org/)
686 [-tools.org/](https://www.generic-mapping-tools.org/)
- 687 Wéber, Z. (2006, May). Probabilistic local waveform inversion for moment tensor and
688 hypocentral location. *Geophysical Journal International*, 165(2), 607–621. Retrieved
689 2021-06-21, from [https://academic.oup.com/gji/article-lookup/doi/10.1111/](https://academic.oup.com/gji/article-lookup/doi/10.1111/j.1365-246X.2006.02934.x)
690 [j.1365-246X.2006.02934.x](https://academic.oup.com/gji/article-lookup/doi/10.1111/j.1365-246X.2006.02934.x) doi: 10.1111/j.1365-246X.2006.02934.x
- 691 Xie, Y., Bao, H., & Meng, L. (2021, October). Source Imaging With a Multi-Array Local
692 Back-Projection and Its Application to the 2019 M_w 6.4 and M_w 7.1 Ridgecrest
693 Earthquakes. *Journal of Geophysical Research: Solid Earth*, 126(10). Retrieved 2021-
694 11-09, from <https://onlinelibrary.wiley.com/doi/10.1029/2020JB021396> doi:
695 10.1029/2020JB021396
- 696 Xu, X., Sandwell, D. T., & Smith-Konter, B. (2020, July). Coseismic Displace-
697 ments and Surface Fractures from Sentinel-1 InSAR: 2019 Ridgecrest Earth-
698 quakes. *Seismological Research Letters*, 91(4), 1979–1985. Retrieved 2021-
699 11-09, from [https://pubs.geoscienceworld.org/ssa/srl/article/91/4/1979/](https://pubs.geoscienceworld.org/ssa/srl/article/91/4/1979/580045/Coseismic-Displacements-and-Surface-Fractures-from)
700 [580045/Coseismic-Displacements-and-Surface-Fractures-from](https://pubs.geoscienceworld.org/ssa/srl/article/91/4/1979/580045/Coseismic-Displacements-and-Surface-Fractures-from) doi: 10.1785/
701 0220190275
- 702 Yue, H., Sun, J., Wang, M., Shen, Z., Li, M., Xue, L., ... Lay, T. (2021, September).
703 The 2019 Ridgecrest, California earthquake sequence: Evolution of seismic and aseis-
704 mic slip on an orthogonal fault system. *Earth and Planetary Science Letters*, 570,
705 117066. Retrieved 2021-11-09, from [https://linkinghub.elsevier.com/retrieve/](https://linkinghub.elsevier.com/retrieve/pii/S0012821X21003216)
706 [pii/S0012821X21003216](https://linkinghub.elsevier.com/retrieve/pii/S0012821X21003216) doi: 10.1016/j.epsl.2021.117066

1 **Supplementary Figures**

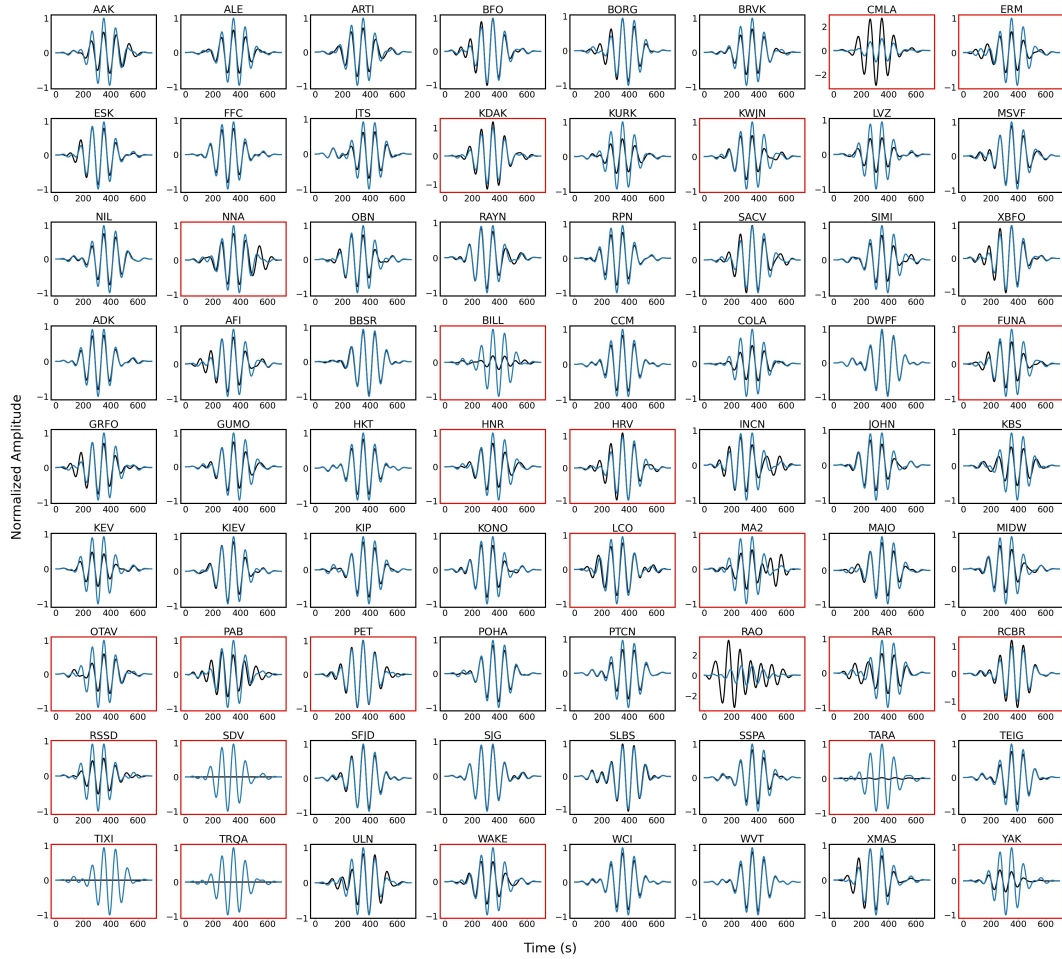


Figure S1. Traces of stations submitted to manual quality control in this study. Station plots with black outlines indicate stations that were kept. Station plots with red outlines indicate stations that weren't kept

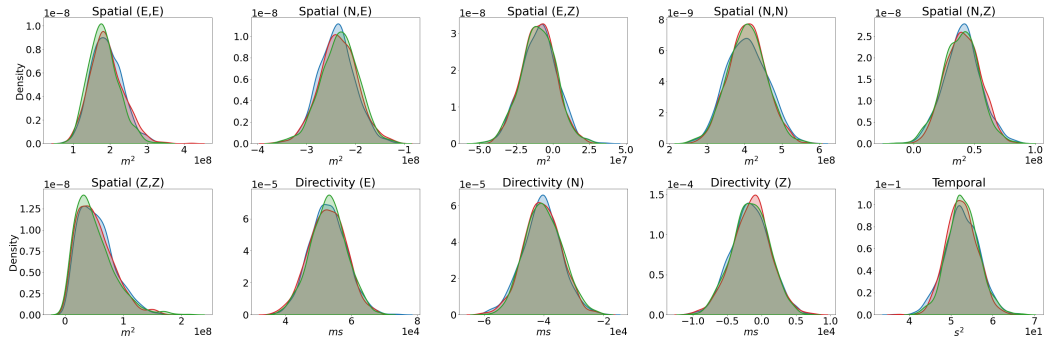


Figure S2. Kernel density estimate plots for multiple chains describing the distributions of independent components of the second moments of the stress glut for the 2019 Ridgecrest sequence mainshock. Different colors (blue, red, and green) represent different chains of the inversion.

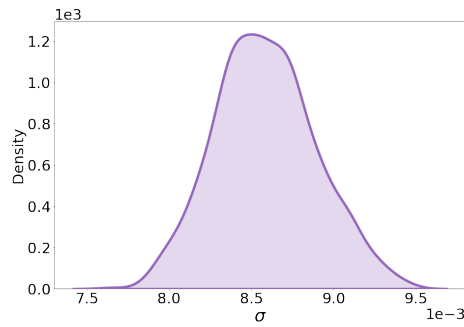


Figure S3. Distribution of hyperparameter σ determined in the inversion using real data and included in the inversion using synthetic data.